

## ARTICLE OPEN



# Visualizing oxygen transport pathways during intergranular oxidation in Ni-Cr

Martin Weiser<sup>1,2</sup>✉, Matthew J. Olszta<sup>2,4</sup>, Mark H. Engelhard<sup>1,3,4</sup>, Zihua Zhu<sup>1,3,4</sup> and Daniel K. Schreiber<sup>1,2,4</sup>

The transport paths of O during intergranular oxidation in binary Ni-Cr were investigated. To isolate the selective oxidation of Cr, oxidation was performed with a CO/CO<sub>2</sub> gas mixture in which the oxygen partial pressure was kept under the NiO dissociation pressure. A combination of electron microscopy and atom probe tomography (APT) was used to study the nanometer-scale details of the passivation and penetrative intergranular oxidation processes at high-energy grain boundaries. Oxygen transport towards the terminating oxidation front is elucidated with dedicated usage of oxygen tracer exchange experiments. Secondary ion mass spectroscopy and APT support classical theories of internal oxidation, revealing preferred transport paths at the oxide/alloy interface with sub-nanometer resolution.

*npj Materials Degradation* (2023)7:70; <https://doi.org/10.1038/s41529-023-00387-w>

## INTRODUCTION

Various Ni-base alloys rely on the formation of protective oxide scales to enhance their durability in applications at elevated temperatures. On the other hand, exposure of similar alloys with an insufficient concentration of desirable oxide-forming elements (e.g., Cr, Al), can lead to fast internal oxidation with concomitant negative effects on the material performance and mechanical properties<sup>1–3</sup>. Even with sufficiently high concentrations of these alloying elements, severe localized attack can result from the local loss of initially protective behavior. In these cases, internal oxidation can be detrimental to material lifetimes in oxidizing atmospheres at intermediate and high temperatures<sup>4,5</sup>.

In 1959, an idealized treatment to predict the transition from internal oxidation towards the growth of a continuous protective layer<sup>6</sup>. Besides the free energy of formation, diffusivities of elements and the solubility of O are important parameters that predict the oxidation behavior of alloys<sup>6,7</sup>. Although various studies investigated and discussed internal oxidation phenomena in detail for decades, conclusive evidence of the exact oxygen transport paths is still missing. The usage of Rhines packs is a dedicated approach to isolate internal oxidation by reducing the oxygen partial pressure below the equilibrium dissociation pressure of the base metal and its pure oxides (e.g., Ni/NiO)<sup>8</sup>. Stott and co-workers followed this strategy to investigate the internal oxidation of binary Ni alloys with up to 5 wt.% of alloying elements<sup>9</sup>. Faster internal oxidation in diluted Ni-Al and Ni-Cr alloys was attributed to accelerated oxygen transport along the interfaces between alloy and internal oxide precipitate<sup>9,10</sup>. For binary Ni-Cr alloys exposed at low oxygen partial pressures, the morphology of oxidation attack ranges from continuous oxides and/or formation of discrete oxide precipitates<sup>11–13</sup>, depending on the parameters of exposure. Besides transport, a second crucial mechanism in Wagner's theory of internal oxidation is the supersaturation of oxygen, which has been more difficult to verify and quantify experimentally. A recent atom probe tomography (APT) study by Poplawsky et al. took an important step in this direction by revealing the enrichment of oxygen on grain

boundaries (GBs) in pure Ni below the oxidation front<sup>14</sup>. However, the measured O concentration was surprisingly low, which indicates the need to revise classical model descriptions.

For Ni-base alloys, diffusion along GBs and other interfaces represents a particularly important mechanism during oxide scale growth in the intermediate temperature range (32–600 °C)<sup>15–17</sup>. More generally, this temperature regime corresponds to type B or C diffusion<sup>18</sup>, in which matrix diffusion is essentially frozen out. Owing to the enhanced transport of both, oxygen and alloying elements, detrimental corrosion scenarios are known to originate and proceed preferentially along GBs and interfaces. For example, intergranular (IG) oxidation is oftentimes a precursor to the initiation of stress corrosion cracking (SCC)<sup>19–21</sup>. Similarly, heat treatment of Cr-containing alloys can lead to the severe local depletion of Cr that sensitizes the material to SCC by inhibiting protective oxide formation<sup>22,23</sup>.

In both internal and IG oxidation, a detailed understanding of elemental transport is critical to elucidating the controlling mechanisms of corrosion. Two-stage exposure to oxygen isotopes (first <sup>16</sup>O<sub>2</sub> and subsequently <sup>18</sup>O<sub>2</sub>) is an effective approach to visualize the transport paths of oxygen. Since labeled (<sup>18</sup>O) isotopes are only present during the second step, their distribution directly informs the dominant oxygen transport pathways and reaction sites relative to the initially formed oxide (<sup>16</sup>O) through the growing oxide scale. The majority of classical approaches for two-stage oxidation experiments used secondary ion mass spectroscopy (SIMS)<sup>17,24–26</sup> or secondary neutral mass spectroscopy (SNMS)<sup>27,28</sup> to analyze the distribution of labeled oxygen. While powerful in interrogating the isotopic distribution as a function of depth, neither technique possesses sufficient lateral resolution to investigate the three-dimensional distribution of oxygen isotopes through the oxide layer(s). To do so, we have deployed APT after two-stage oxidation experiments to directly visualize the 3D O isotope distribution accompanying IG oxidation of diluted Ni-Cr alloys. Another important contribution demonstrated the usage of an <sup>18</sup>O tracer together with high-resolution analysis to elucidate the propagation of oxide growth along GBs below crack tips<sup>29</sup>. Similar to the Rhines pack method, the present

<sup>1</sup>Institute I: General Materials Properties, Friedrich-Alexander-Universität Erlangen-Nürnberg, Martensstrasse 5, 91091 Erlangen, Germany. <sup>2</sup>Energy and Environment Directorate, Pacific Northwest National Laboratory, Richland, WA 99352, USA. <sup>3</sup>Environmental and Molecular Sciences Laboratory, Pacific Northwest National Laboratory, Richland, WA 99352, USA. <sup>4</sup>These authors contributed equally: Matthew J. Olszta, Mark H. Engelhard, Zihua Zhu, Daniel K. Schreiber. ✉email: martin.weiser@fau.de

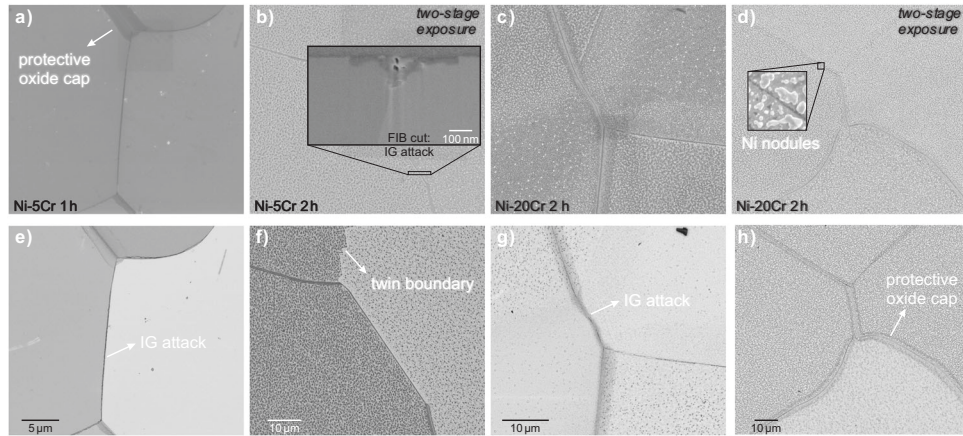


**Fig. 1** Micrographs of Ni-Cr model alloy surfaces after exposure at 600 °C in CO-CO<sub>2</sub>. **a, b** SE micrographs of Ni-5Cr. **c, d** SE micrographs of Ni-20Cr. **e, f** BSE micrographs of identical regions (Ni-5Cr) as in top row. **g, h** BSE micrographs of identical regions (Ni-20Cr) as in top row. Specimens after two-stage exposures are indicated. Inset images show, respectively, a FIB-SEM cross-section view of IG attack (**b**) and a higher magnification of extruded Ni nodules (**d**) on the oxidized sample surface.

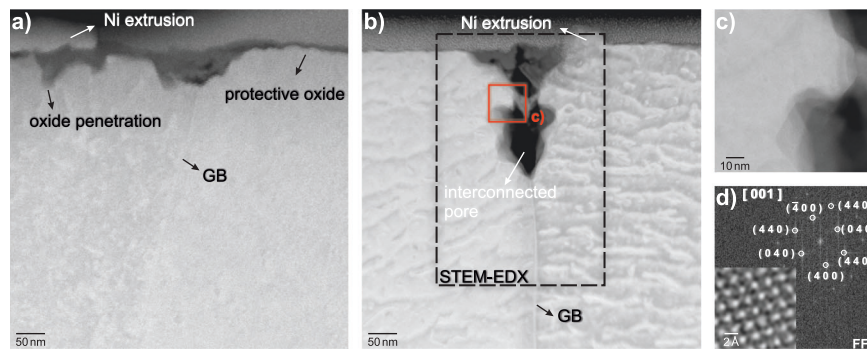


**Fig. 2** STEM-HAADF micrographs of representative GB regions in Ni-5Cr after 1 h exposure at 600 °C. **a** Protected GB. **b** Internally attacked GB. **c** Detailed view on oxide region that is indicated in **b**. **d** FFT of the displayed region and corresponding Cr<sub>2</sub>O<sub>3</sub> lattice reflection with high-resolution electron micrograph as inset.

study uses a controlled oxygen potential via a mixture of CO/C<sup>18</sup>O<sub>2</sub> gas to bias the system towards selective oxidation of Cr and IG oxidation. By monitoring the penetration and distribution of <sup>18</sup>O from C<sup>18</sup>O<sub>2</sub> using APT, we can directly observe short-circuit diffusion of <sup>18</sup>O towards the oxidation front along the IG oxide/metal interface.

## RESULTS

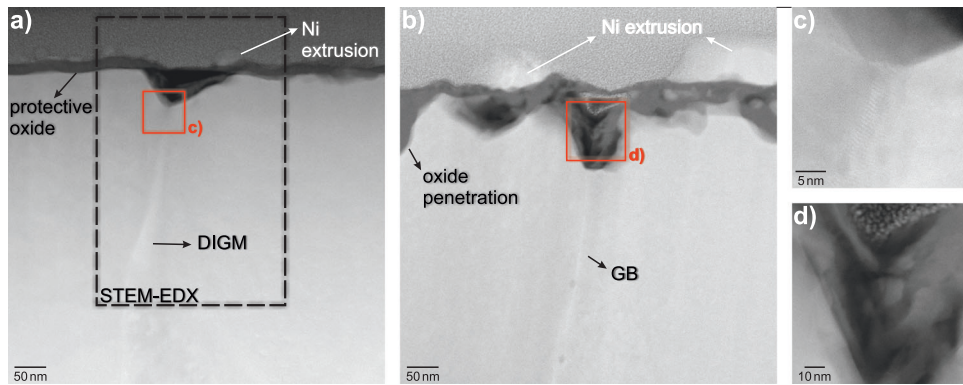
### Morphology of oxide scales formed during exposure in CO-CO<sub>2</sub> mixtures at 600 °C

Figure 1 displays SEM micrographs of representative surface regions of Ni-Cr model alloys after exposure to a CO-CO<sub>2</sub> mixture at 600 °C. The same locations are characterized with SE and BSE contrast to demonstrate as many details as possible.

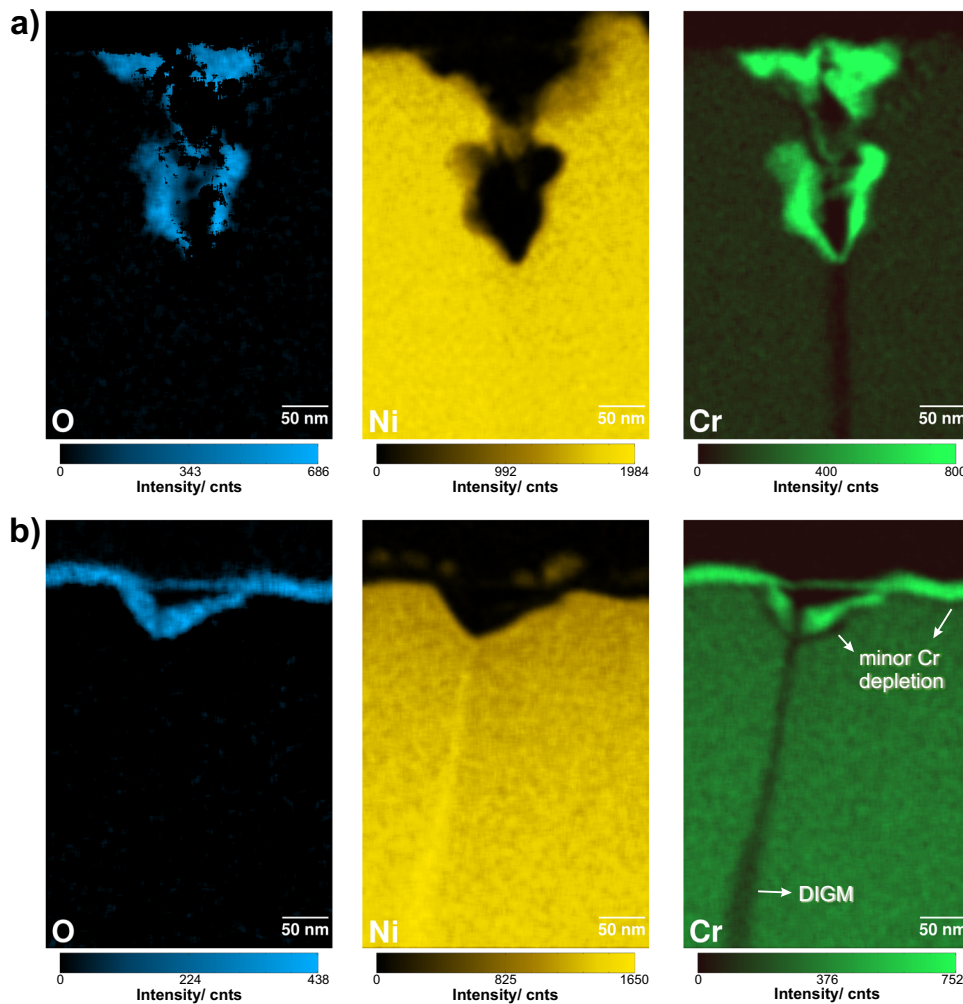
The focus lies on the appearance of GBs and directly adjacent regions. All specimens demonstrated comparable oxidation behaviors, with significant oxidation confined to regions close to GBs. Depending on the individual GB, the width of the surface oxide varies significantly. FIB cross-sections (inserts Fig. 1b) indicated that GBs that demonstrate a narrow dark contrast in the BSE micrographs were attacked by penetrative IG oxidation, while a wider stretch of surface oxide correlates with a protective oxide preventing penetrative oxidation along GBs. The latter revealed minor penetration of IG oxide phases, less than 50 nm below the original surface. Consequently, these GB with broader dark-appearing oxide caps were classified as protected GBs (e.g.,

Fig. 1a, h). After 1 h exposure, the width of these protective oxide caps is asymmetric, spreading further into one adjacent grain over the other. Lateral extensions of protective GB oxide phases appear less dependent on the grain orientation after 2 h exposure to CO-CO<sub>2</sub>. Additionally, it has to be noted that low-energy (twin) boundaries did not exhibit any oxidation. Consequently, no significant oxide on the surface of these characteristic interfaces could be recognized from top view SEM micrographs (Fig. 1f). The grain interiors are covered by bright-appearing features. These nearly circular phases on the surface can be identified as Ni nodules that have already been observed in previous oxidation studies performed in atmospheres with particularly low  $p_{O_2}$ <sup>11</sup>. The classical oxidation theory associates the growth with metallic nodules on the surface of binary alloys with considerable internal oxidation and associated internal stress<sup>30</sup>. The density of these features increases with the time of exposure.

Site-specific TEM samples were prepared for a more detailed consideration of elemental distribution in oxidation-affected regions. Figure 2 displays high-angle annular dark-field (HAADF) micrographs of a Ni-5Cr GB that is protected by Cr<sub>2</sub>O<sub>3</sub> and one GB that formed IG oxides after 1 h exposure at 600 °C. The protective oxide (Fig. 2) spreads laterally along the sample surface of both adjacent grains. The oxide layer covering the left grain is thicker than that formed on the opposite grain. To a minor extent, oxide penetrations (depth > 50 nm) at both termination sides are visible. However, the micrograph only displays the penetration of the protective oxide into the interior of the left grain. Above the oxide are extruded Ni-rich nodules that exhibit a bright contrast in



**Fig. 3** STEM-HAADF micrographs of representative GB regions in Ni-20Cr after exposure at 600 °C. **a** GB with protective oxide cap after 1 h in natural CO/CO<sub>2</sub>. **b** Internally attacked GB after two-stage exposure (2 h). **c, d** Detailed view on oxide directly below the crack.



**Fig. 4** Elemental distribution maps of O, Ni, and Cr taken from regions marked in STEM-HAADF micrographs of Ni-Cr model alloys after exposure for 1 h at 600 °C. **a** IG attack in Ni-5Cr and **b** protected GB in Ni-20Cr.

HAADF imaging. The GB below the oxide cap appears unaltered in the HAADF image. Figure 2b–d demonstrates the morphology of a GB exhibiting IG oxidation. As suggested from the top view SEM images, no significant oxide formed across the exposed surface. Instead, a porous IG oxide extends  $\approx 220$  nm into the GB (Fig. 2b). Tilt series (shown in the supplementary material) demonstrated the interconnected nature of the porosity. The interface of the IG oxide with the left alloy grain is displayed in higher magnification

in Fig. 2c, d. Fast Fourier transformed (FFT) of the atomically resolved HAADF is consistent with an  $M_2O_3$  structure, and likely  $Cr_2O_3$ .

For comparison, representative regions of Ni-20Cr specimens after exposure at 600 °C in CO-CO<sub>2</sub> were analyzed in the TEM. The micrographs in Fig. 3 display a protected GB after 1 h exposure and IG oxidation in a sample after 2 h total exposure during tracer exchange experiments. Generally, the Cr concentration of 20 at.%

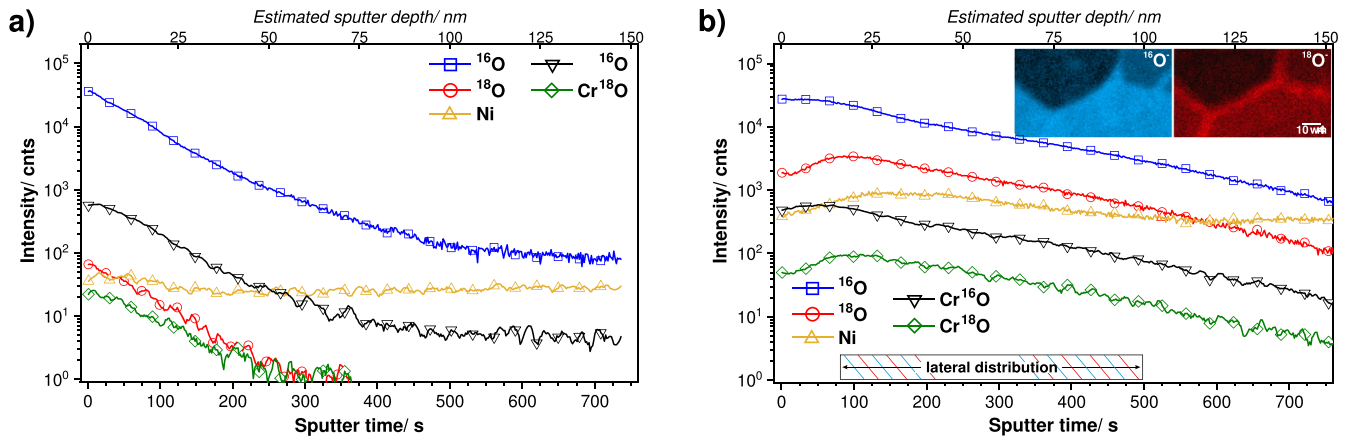


**Fig. 5** Depth profiles (ToF-SIMS) of Ni-20Cr samples after. **a** 1 h exposure in natural CO-CO<sub>2</sub> mixture and **b** two-stage tracer exchange exposure in CO-C<sup>16</sup>O<sub>2</sub> (40 min) and CO-C<sup>18</sup>O<sub>2</sub> (80 min). Insets in **b** show the lateral distribution of cumulated O intensities.

Cr leads to a higher number of protected than unprotected GBs, although the response is qualitatively quite comparable with the 5 at.% Cr oxidation. However, the displayed surface oxide is thicker compared to the one found on Ni-5Cr specimens, while the IG oxidation is shallower. Porosity developed in the region directly above the GB. Additionally, diffusion-induced grain boundary migration (DIGM) can be recognized in the HAADF image (Fig. 3a). The protective oxide layer on the Ni-20Cr sample (Fig. 3a) developed during the same length of exposure as the one displayed for Ni-5Cr (Fig. 2a). The internal oxidation front (IOF) penetrated ≈60 nm into the alloy. Both, the protective as well as the IG oxide, reveal considerable porosity, and a comparably thick surface oxide formed on top of the displayed IG oxidized GB (Fig. 2b). The increase of oxidation time caused a thicker surface oxide over a comparably wide section. The IOF terminates ≈ 140 nm below the surface. For each cross-section, a region directly below the pore in the IG oxide is displayed with higher magnification in Fig. 3c, d. Oxide at the termination of the protective cap penetrated both grains and reached a comparable depth as the IG oxide section along the GB. The surface of the Ni-20Cr sample is also covered with Ni nodules that nearly reach the region directly above the GB.

Additional STEM-EDX data were collected for representative regions of Ni-5Cr and Ni-20Cr after 1 h oxidation, as indicated in the HAADF micrographs (Figs. 2b and 3a). The resulting elemental distribution maps of O, Ni, and Cr are displayed in Fig. 4.

During IG oxidation of Ni-5Cr, the majority of Cr is supplied along the GB. High intensities of O do not exhibit considerable Ni enrichment, which excludes the formation of Ni-Cr spinel oxides. Both Ni maps confirm Ni nodules extrusion above the oxide layers, as speculated about previously in Fig. 1). Directly below the IOF, the Cr-depleted zone that surrounds the GB of the Ni-5Cr sample exhibits a width of ≈ 20 nm. This is broader than in the protected GB of the Ni-20Cr sample (≈ 12 nm) at the same depth. Additionally, Cr depletion adjacent to the lateral sections of the GB is recognizable in both grains of the Ni-20Cr sample. This finding indicates that lattice diffusion of Cr occurs at the considered temperature, however to a limited extent. The elemental distribution adjacent to the selectively oxidized GB of Ni-20Cr (Fig. 3b) during tracer exchange experiments in the CO-CO<sub>2</sub> mixture was also investigated by means of STEM-EDX. Detailed results can be found elsewhere<sup>31</sup>. Again, Cr depletion is confined to the GB. However, the grain interiors adjacent to the oxide do not indicate any significant depletion in Cr. The growth of Cr<sub>2</sub>O<sub>3</sub> has to be sustained by a Cr flux along the GB. In both cases, Ni is enriched along the GB as a consequence of Cr consumption during oxidation. With the demonstrated conventional electron microscopic analysis we confirm that the current

experimental conditions evoke selective IG oxidation of Cr at select GBs in both Ni-Cr alloy compositions. In the next section, we further investigate these behaviors using isotopic tracers in the two-stage oxidation method.

### Oxygen tracer exchange in CO/CO<sub>2</sub> mixture at 600 °C

Two-stage isotopic tracer exchange experiments with labeled C<sup>18</sup>O<sub>2</sub> were conducted at 600 °C to visualize O diffusion paths during IG oxidation. ToF-SIMS depth profiles were first recorded to document the average depth profile of the <sup>18</sup>O incorporation. Figure 5 shows the measured intensity for relevant ion signal intensities versus sputter time for Ni-20Cr after 1 h with no <sup>18</sup>O introduction and a total of 2 h in the two-stage <sup>16</sup>O/<sup>18</sup>O oxidation. Since the morphological investigation indicated an inhomogeneous depth of oxide penetration, the sputtering time was not calibrated. Therefore, no specific (sputter) depth for the elucidated model alloys is given in the figure. For the applied Bi<sub>3</sub><sup>++</sup> beam characteristics (50 keV acceleration voltage and 77 nA beam current), the sputter rate on a pure Ni sample can be approximated with 0.20 ± 0.01 nm/s.

The selection of conclusive components of the SIMS signals can be quite tedious for complex oxides that developed in gaseous atmospheres. TEM-EDX confirmed Cr<sub>2</sub>O<sub>3</sub> as the only relevant oxide phase that needs to be considered after exposure to binary Ni-Cr alloys in CO-CO<sub>2</sub> mixtures. Intensity (depth) profiles of <sup>52</sup>Cr<sup>16</sup>O<sup>-</sup> and <sup>52</sup>Cr<sup>18</sup>O<sup>-</sup> (68 and 70 Da) are shown along with peaks for the two most-abundant oxygen ions (<sup>16</sup>O<sup>-</sup> and <sup>18</sup>O<sup>-</sup>) at *M/e* values of 16 and 18 Da. Owing to the significantly lower isotopic abundance of <sup>54</sup>Cr (0.024) compared to <sup>52</sup>Cr (0.838), the peak at 70 Da can be attributed to labeled <sup>52</sup>Cr<sup>18</sup>O<sup>-</sup> with sufficiently high confidence. As Ni did not exhibit meaningful oxidation under these low *p*<sub>O<sub>2</sub></sub> conditions, the Ni<sup>-</sup> signal (58 Da) can be used to represent the substrate. The increase of the Ni signal indicates the transition to mostly oxygen-free sample regions below the IOF of the included GBs. This was similarly suggested in previous work that used ToF-SIMS to characterize oxide layer growth on Ni-Cr alloys<sup>26</sup>.

After 1 h oxidation in CO-CO<sub>2</sub>, the Ni-20Cr sample did not exhibit significant surface oxide apart from the protective Cr<sub>2</sub>O<sub>3</sub> cap that covered certain GBs. Consequently, a maximum in the Ni<sup>-</sup> signal is visible after ≈ 58 s of sputtering in Fig. 5a. The intensity maximum of CrO<sup>-</sup> lies at ≈ 30 s of sputtering. Increasing the oxidation time to 2 h resulted in considerably thicker surface oxides as demonstrated with STEM-EDX. Consequently, the intensity maxima of Cr<sup>16</sup>O<sup>-</sup> (≈ 52 s) and Ni (≈ 141 s) were detected after longer sputtering times. Even more interesting is the depth distribution of labeled <sup>18</sup>O in the ToF-SIMS data. Figure 5b indicates clear maxima of <sup>18</sup>O<sup>-</sup> and Cr<sup>18</sup>O<sup>-</sup> signals after ≈ 95 s of sputtering. Since only the atmosphere

of the second stage of exposure contained a significant  $^{18}\text{O}$  content, this shows that O has diffused through the pre-formed  $^{16}\text{O}$  oxide to the deeper IOF. Additionally, the lateral distribution of  $^{16}\text{O}^-$  and  $^{18}\text{O}^-$  was analyzed in more detail. The insets in Fig. 5b show the intensity distribution of the 16 Da (blue) and 18 Da (red) peaks between 60 and 500 s sputtering. Significant  $^{18}\text{O}^-$  signal is confined along GBs, showing  $^{18}\text{O}$  penetration to the leading IG oxidation front.

The deliberate deviation from the natural isotopic abundance of oxygen during the second stage of the oxidation experiments added complexity to the interpretation of APT mass spectra. A custom treatment of the APT mass spectra was therefore needed. Figure 6 shows typical mass spectra that were collected after 1 h

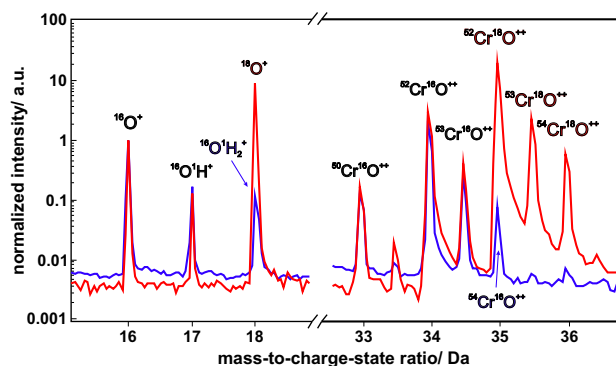


**Fig. 6** Representative mass spectra of Ni-5Cr after exposure to natural (blue) and labeled (red)  $\text{CO}/\text{CO}_2$  600°C. Colored labels indicate species that are only included in the respective dataset.

exposure to natural  $\text{CO}-\text{CO}_2$  and after 2 h tracer exchange experiments with labeled ( $\text{CO}-\text{C}^{18}\text{O}_2$ ) oxygen. Intensities for both datasets were normalized to the  $^{16}\text{O}$  peak.

For both datasets (Fig. 6), the peak at 16 Da can unambiguously be allocated to  $^{16}\text{O}^+$ . The mass spectra after exposure to isotopically labeled  $\text{C}^{18}\text{O}_2$  exhibit a significantly increased peak intensity at 18 Da. The relative peak intensities at 17 Da are nearly identical and can therefore be allocated to  $^{16}\text{O}^1\text{H}^+$ . In contrast, the peak at 18 Da after two-stage exposure exceeds the  $^{16}\text{O}^1\text{H}^{++}$  natural abundant oxide by two orders of magnitude. This is an explicit indication of the presence of labeled oxygen in the dataset. Additionally, it was stated in the literature, that a significantly higher 18 Da peak without considerable contribution at 17 Da excludes the formation of  $\text{O}_2^{++32}$ . Since combinations of Cr isotopes with both  $^{16}\text{O}$  and  $^{18}\text{O}$  have to be examined the treatment becomes complex. Peaks are indicated that correspond to contributions from  $\text{CrO}^{++}$  ions with the distinctions of all isotopes are indicated in Fig. 6. Since combinations of Cr isotopes with both  $^{16}\text{O}$  and  $^{18}\text{O}$  have to be examined the treatment becomes complex. For more details, the reader is referred to the supplementary section of the paper. After considering contributions from the most-abundant Cr and O isotopes the expected exclusive growth of  $\text{Cr}_2\text{O}_3$  in the investigated APT data can be confirmed. Furthermore, the applied procedure for peak identification delivers relevant and accurate information about the distribution of natural and labeled contributions in the  $\text{Cr}_2\text{O}_3$  region.

After reconstruction, the distribution of  $\text{Cr}^{16}\text{O}$  and  $\text{Cr}^{18}\text{O}$  along with Ni is represented as 3D ion maps. Figure 7a displays the oxide alloy interface of Ni-5Cr after two-stage exposure in the  $\text{CO}-\text{CO}_2$  mixture. For a more detailed analysis of the interface between oxide and alloy, a 6 at.% O isoconcentration surface was

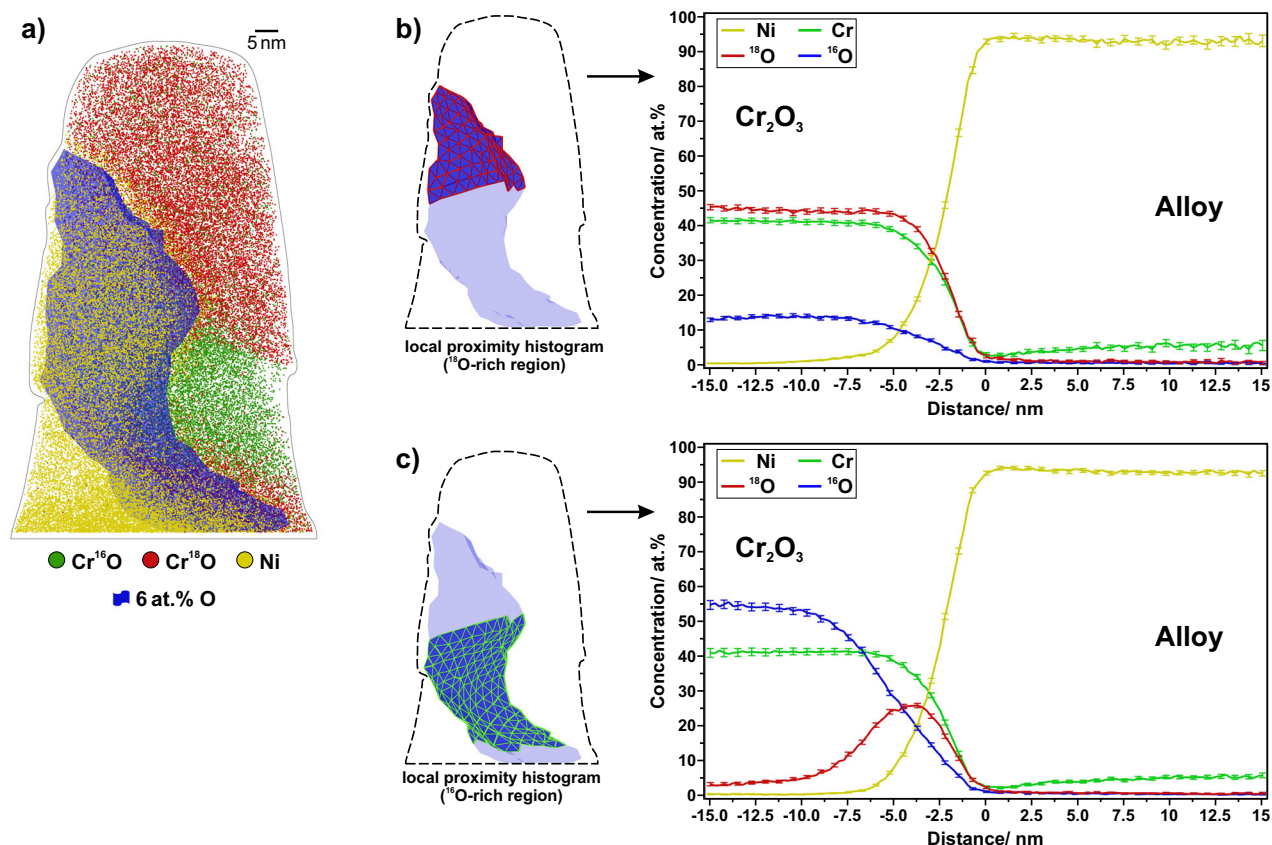


**Fig. 7** APT analysis of Ni- $\text{Cr}_2\text{O}_3$  interface in Ni-5Cr after 2 h oxidation at 600°C in  $\text{CO}/\text{CO}_2$  mixture. 3D reconstruction (a) and local proximity histograms (b, c) considering different regions of the displayed O isoconcentration surface (6 at.%).

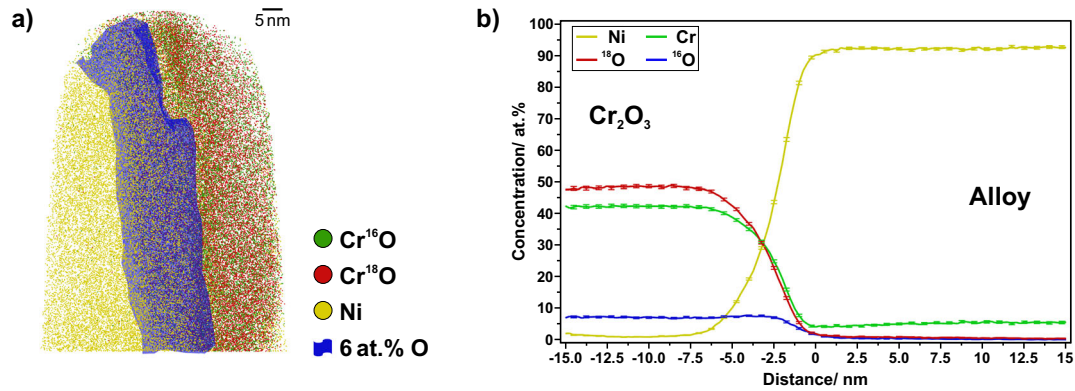


**Fig. 8** APT analysis of Ni-Cr<sub>2</sub>O<sub>3</sub> interface in Ni-5Cr after 2 h two-stage oxidation at 600 °C in CO/CO<sub>2</sub> mixture. **a** APT atom map with a 6 at.% O isoconcentration surface separating the oxide and metal, and **b** corresponding proximity histogram.

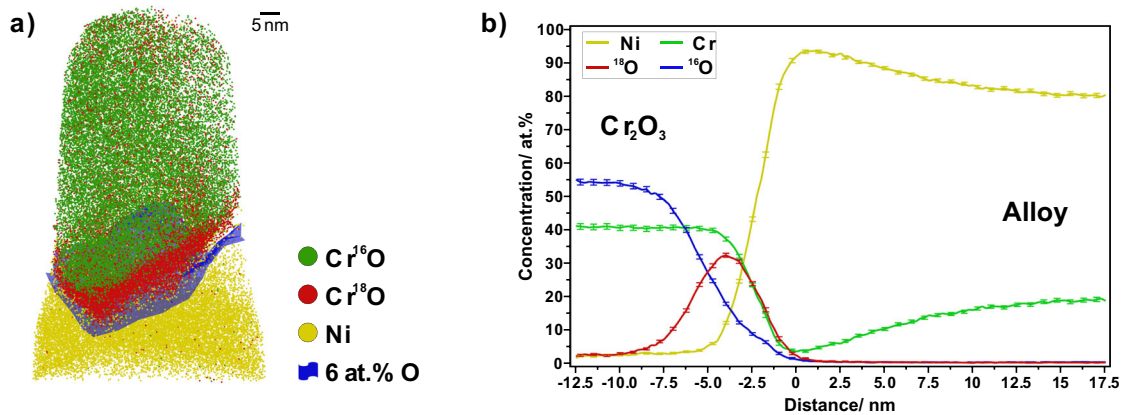


**Fig. 9** APT analysis of Ni-Cr<sub>2</sub>O<sub>3</sub> interface in Ni-20Cr after 2 h oxidation (600 °C) in CO/CO<sub>2</sub> mixture. 3D reconstruction (**a**) and local proximity histogram (**b**) of the displayed O isoconcentration surface (6 at.%).

computed. To determine an accurate surface, the dataset was decomposed and all O contributions (<sup>16</sup>/<sup>18</sup>O) were considered. Towards the bottom of the reconstruction, the oxygen signal is dominated by contributions from Cr<sup>18</sup>O (green dots), whereas the upper region is highly enriched in Cr<sup>18</sup>O (red dots). Therefore, the displayed sample volume contains oxide that grew during the first stage (<sup>16</sup>O-rich) and oxide that formed during the second stage with a considerable <sup>18</sup>O from the atmosphere. To elucidate the concentration changes across the oxide/alloy interface, local proximity histograms were calculated (Fig. 7b, c). The isoconcentration surface was subdivided manually into one section that separates the alloy and Cr<sup>16</sup>O-rich region and a second section between alloy and oxide that grew during exposure to CO-C<sup>18</sup>O<sub>2</sub>. The conducted workflows to compute local proximity histograms from a curved interface were adapted from Felner et al.<sup>33,34</sup>. The surface was composed of a mesh of individual vertices (307 in Fig. 7) to calculate the “local” proximity histogram, only vertices adjacent to the region of interest are considered. For more details, the reader is referred to the original publications. To gain a visual impression of the lateral distribution of considered vertices (and triangulated faces), the isoconcentration surface is displayed along with the underlying mesh. The 93 vertices that were used to calculate proxigrams for the <sup>18</sup>O-rich regions are displayed in the same color (red) as Cr<sup>18</sup>O ions, whereas the remaining vertices are drawn in the color (green) of Cr<sup>16</sup>O ions.

The proximity histogram in Fig. 7b indicates a locally homogeneous distribution of <sup>16</sup>O and <sup>18</sup>O through the oxide, at an <sup>18</sup>O concentration of 45 at.%. Combining the contributions of <sup>16</sup>O and <sup>18</sup>O, the net oxygen concentration is approximately 60 at.%, which is consistent with the expected value for chromia. The high <sup>18</sup>O

contribution also is consistent with an interpretation that this region formed during the second stage of the exposure. Both proximity histograms indicate only minor depletion of Cr (≈ 2 at.%) in the alloy region directly adjacent to the alloy/oxide interface. The second proximity histogram shown in Fig. 7c reveals a more complicated behavior where <sup>18</sup>O enrichment exists for ≈ 8 nm directly against the oxide/metal interface. This zone with increased contribution of labeled oxygen is hard to locate in the ion distribution map.

APT analysis of the internal alloy/oxide interface of a second sample volume is shown in Fig. 8. The targeted region was near the IOF. In this dataset, the entire IG oxide volume is homogeneously enriched in <sup>18</sup>O. A proximity histogram from the 6 at.% O isoconcentration surface (Fig. 8b) shows no apparent enrichment of <sup>18</sup>O at the oxide/metal interface. The Cr/O ratio (≈ 2:3) matches the expected ratio for Cr<sub>2</sub>O<sub>3</sub>. A weak depletion of Cr over approximately 6 nm can be seen in the alloy. However, the significant concentration of Cr directly at the interface (≈ 2 at.%) indicates a negligible contribution of Cr transport from the alloy to sustain oxide growth.

Further APT analysis on IG oxides in Ni-20Cr after two-stage exposure was conducted to verify if comparable O transport paths are present in alloys with a higher concentration of the alloying element. Particularly interesting is the interface between alloy and oxide phases that grew during exposure in CO-CO<sub>2</sub> atmospheres with natural O abundance (e.g., Fig. 7c) since the enrichment of labeled oxygen suggests an important role during inward O transport. Figure 9 displays a representative APT analysis of an equivalent sample volume in the Ni-20Cr model alloy.

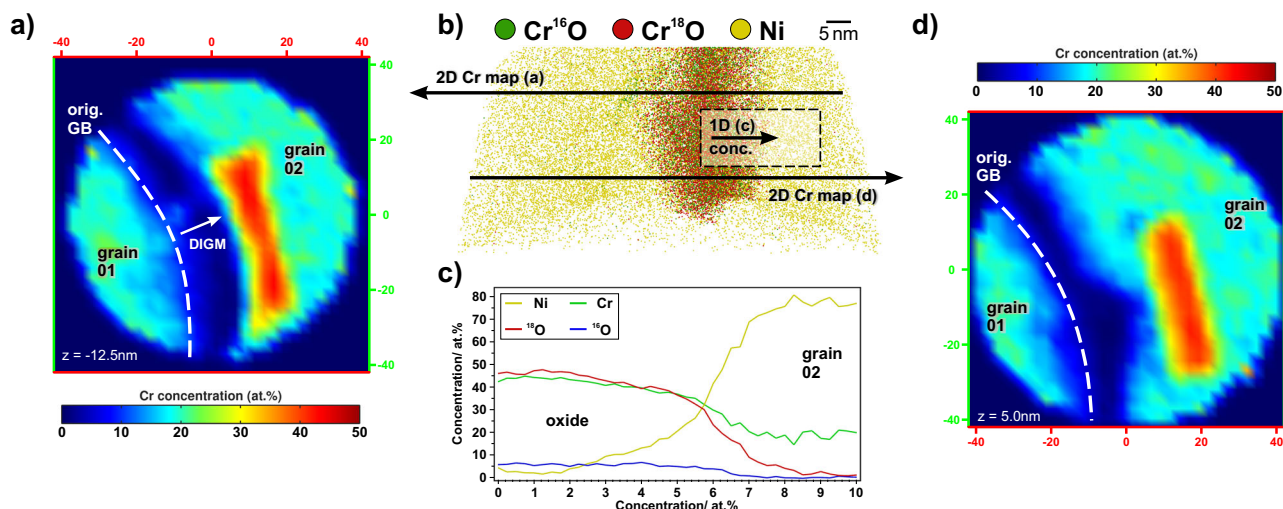


**Fig. 10** APT data from oxide termination adjacent to a Cr-depleted GB. APT data from oxide termination adjacent to a Cr-depleted GB. Cr concentration maps (a, d) were calculated with a bin width of 2.5 nm and perpendicular to the direction of the analysis. The arrows in the reconstruction (b) indicate the respective positions in the data set as well as 1D concentration profiles (c).

The IG oxide can be subdivided into two parts. One section contains a considerable  $^{16}\text{O}$  signal and therefore developed within the first 40 min of exposure (natural O abundance). A narrow region of newly formed oxide is located directly adjacent to the interface. As stated above,  $\text{Cr}_2\text{O}_3$  with significantly enriched  $^{18}\text{O}$  content can only grow during the second stage of the experiment. This is an additional verification for preferential inward O transport along the interface between alloy and oxide.

The proximity histogram, displayed in Fig. 9b, quantitatively confirms the visual impression from the ion map. The newly formed  $^{18}\text{O}$ -rich oxide layer extends for 8–10 nm between the alloy and  $\text{Cr}_2^{16}\text{O}_3$ . The proximity histogram reveals a clear depletion of Cr in the adjacent alloy. The Cr-depleted zone spreads over approximately 15 nm into the base alloy. Interestingly, the Cr concentration directly at the interface remains at a level of 2 at.%. This minimum in Cr concentration is comparable to the values measured for alloy/oxide interfaces in APT data from Ni-5Cr samples.

3D APT data from a different specimen that includes the IG oxide section directly above the IOF is shown in Fig. 10b. The displayed terminating portion is expected to be 10 nm above the IOF. Contributions of  $\text{CrO}^{+3}$  ions that originate from the most-abundant oxygen isotopes,  $^{16}\text{O}$  and  $^{18}\text{O}$ , are displayed with different colors in the ion map. Two 2D concentration maps of the Cr distribution are presented from different depth slices of the reconstruction in Fig. 10a, d.

The terminal IG  $\text{Cr}_2\text{O}_3$  is adjacent to a grain boundary and is 18–20 nm thick. A 1D concentration profile through the oxide section (Fig. 10c) indicates a nearly identical  $^{16}\text{O}/^{18}\text{O}$  ratio in labeled oxides that formed during the second stage in Ni-5Cr (Fig. 8b) and in Ni-20Cr. Once more, the constant high amount of labeled oxygen indicates that the displayed  $\text{Cr}_2\text{O}_3$  section grew during the second stage of the exposure when  $^{18}\text{O}$  was significantly enriched. A most intriguing feature of the present dataset is the included alloy GB. The demonstrated Cr concentration maps (Fig. 10a, d) were calculated from different heights, 17.5 nm apart from each other.

The concentration profile in Fig. 10a originates from a region nearer the exposed alloy surface. A stripe of approximately 14 nm width is completely depleted in Cr ( $< 0.05$  at.%), proving that Cr diffusion through the metal interior is negligible at these exposure temperatures. As a consequence of the rapid transport of Cr along the GB, DIGM initiated<sup>35</sup>. The original location of the GB is approximated by a dashed line in the Cr concentration map. In

addition, the Cr distribution map emphasizes a negligible contribution of Cr diffusion in the matrix. Neither the interface of the chromia with grain02 nor the interface of the original GB with grain01 exhibits a considerable gradient in Cr concentration. Closer to the IOF, the Cr depletion in grain02 appears less regular. Even though, the transition between the depleted region and the matrix is equally sharp, only a section of the IG oxide is connected with the Cr-depleted zone.

## DISCUSSION

The transport of oxygen through a complex surface oxide of a Ni-base alloy after exposure to pressurized water was previously reported<sup>26</sup>. The study underlined the potential of SIMS depth profiling in combination with labeled oxygen isotopes to prove inward transport. However, no conclusive results on the diffusion paths could be reported. The ToF-SIMS analysis presented in Fig. 5 aims to sustain model predictions by providing information on the lateral distribution of the respective oxygen isotopes. The limitations due to the insufficient resolution of the maps demonstrate the importance to use APT for the investigations. The high concentration of  $^{18}\text{O}$  in oxide portions that formed in the vicinity of the IOF (Fig. 10) added further indirect proof for inward oxygen transport. Nevertheless, only a detailed analysis of interfaces between the alloy and oxide phases that formed during the first stage of exposure reveals the transport path. Considerable  $^{18}\text{O}$  enrichment at these interfaces (Figs. 7 and 9).

As outlined above, several acclaimed studies aimed to explain oxygen transport during internal oxidation. Stott et al. reported discrepancies in the relative depth of oxygen penetration from estimated values using bulk diffusivity of oxygen in Ni-Cr system during internal oxidation<sup>9,36</sup>. Considerable enhancement of diffusion along alloy/oxide interfaces was proposed. The model predictions were also adapted by other groups<sup>20</sup> for the unexpectedly fast IG corrosion of Alloy 600 in hydrogenated steam. Nevertheless, direct and unambiguous proof for preferred O diffusion along the interface of internal oxide phases could not be delivered until today. To our knowledge, the demonstrated APT analysis of distinct sample regions after two-stage oxygen tracer exchange is the first visual evidence for the proposed transport mechanism. In more general cases, APT was demonstrated to reveal the enrichment of elements along metal/oxide interfaces that could be connected to elemental transport. For example, the

outward transport of Ni in alloy 600 during severe internal oxidation was proven by Langelier and Co-workers<sup>37</sup>.

Another morphological feature of the formed oxide is the apparent porosity. It cannot be stated with certainty to which extent pore networks developed already during the exposure. In general, interconnected pores could allow the access of molecular species to the oxidation front<sup>38–40</sup>. The phenomena were also observed for IG oxide formed during exposure to hydrogenated water<sup>35</sup>. The diffusion of O along the alloy/oxide interface was unequivocally proven. However, the additional contribution of gaseous transport cannot be excluded.

Cr-depletion in alloy regions adjacent to the oxide interface is scarcely detectable in proximity histograms of Ni5Cr. After 2 h oxidation at 600 °C, samples with 20 at.% exhibit a region of approximately 15 nm length that is depleted in Cr. Closer to the termination of the oxide network, Cr concentration maps (Fig. 10) indicated no apparent consumption of the solute from the matrix. This is interesting since this oxide portion depicts the early stage of IG oxide growth. One possible explanation for the delayed onset of Cr depletion in the alloy could be negligible diffusion of the solute to the surface. In other words, at this stage of oxidation, the Cr flux that arrives at the IOF is immediately consumed by the expansion of IG oxide along the GB. In contrast, the STEM-EDX maps in Fig. 4 of both alloys demonstrate depletion of Cr along the GB. This leads to the conclusion that the majority of Cr originates from the GB far below the IOF. Alloy regions neighboring penetrating oxide in grain interiors of the surface oxides are scarcely depleted in Cr. The formation of Cr<sub>2</sub>O<sub>3</sub> is therefore solely sustained by transport along the GB. In accordance with severe Cr depletion, Ni is enriched along the GB. DIGM was also observed on some of the protected GBs, especially in the Ni-20Cr specimens (Fig. 3). Since the focus of this study was the understanding of O transport, the well-explained mechanism is not considered in detail. Briefly summarized, the short-circuit diffusion of Cr towards the IOF is non-symmetric<sup>35,41</sup>. During consumption of Cr and simultaneous depletion, the GB migrates towards the IG oxide (Fig. 10). For more details, readers are referred to previous studies on the oxidation behavior of Cr-containing alloys in the intermediate temperature regime<sup>41–44</sup>.

The internal oxide scale morphologies in Ni-5Cr and Ni-20Cr samples after oxidation in CO-CO<sub>2</sub> mixtures were consistent. Despite the reduction of O availability, both compositions revealed GBs that were protected by Cr<sub>2</sub>O<sub>3</sub> on the surface as well as GB that were decorated by interconnected IG oxide. Owing to the overall lower Cr reservoir, more GBs were attacked in samples with 5 at.% Cr. Especially GBs below protective oxide caps (Fig. 3a) demonstrated migrated interfaces and were more frequently observed in the alloy with 20 at.% Cr. However, APT analysis of IG oxide termination exhibited traces of a migrated GB (Fig. 10). Literature studies reported DIGM in Ni-5Cr model alloys after long-term exposure (100–1000 h) in hydrogenated water at 330 °C<sup>35,45</sup>. Therefore, it appears plausible to assume that also DIGM will initiate in Ni-5Cr samples at longer oxidation in CO-CO<sub>2</sub>. A particularity of IG attack in Ni-Cr alloys during exposure to hydrogenated water is the formation of oxide branches that reach into the alloy<sup>31,46</sup>. Even though not every IG oxide was only confined to the GB line, apparent growth of oxide branches that reach into the alloy was not observed during our analysis. One reason for the absence of these features might be sufficient Cr supply at 600 °C that ensures expansions along the IG region and thereby prevent the accumulation of growth stresses that would be suspected to cause transgranular expansion of oxide lattices.

For both Cr contents, specimens formed Ni extrusions during IG oxidation. These phases appear homogeneously distributed in individual grains. The density of Ni nodules varies depending on the grain characteristics. Additionally, the surfaces of Ni-20Cr samples exhibited more Ni extrusions than the ones of Ni-5Cr after the same experiments. As initially stated, Ni diffusion to the surface was attributed to intense internal oxidation<sup>11</sup>. Studies that

are more recent also demonstrated extensive growth of metallic Ni extrusions in the course of IG oxidation in hydrogenated steam or water<sup>47–49</sup>. Growth of internal Cr<sub>2</sub>O<sub>3</sub> is suggested to block diffusion of Ni to the termination of GBs on the surface. Additionally, the Ni transport is sustained by the evolution of compressive stress fields within the alloy during volume increase due to oxide growth<sup>37</sup>. These assumptions are also supported by an older study on the internal oxidation of binary Ni alloys under load. At moderate strain rates, Ni-Cr alloys demonstrated an increased Ni flux to the surface and deeper penetration of the (IG) oxidation front<sup>50</sup>. Internal oxidation can occur in Ni-base systems even with very high Cr concentrations. For example, dislocation networks in Alloy 690 (30 at.% Cr) were demonstrated to facilitate O penetration that resulted in the growth of Cr<sub>2</sub>O<sub>3</sub> in grain regions below the surface<sup>51</sup>. The present study could not reveal a significant contribution of further short-circuit pathways, especially sub-surface dislocations. It is emphasized once again, that their relevance is well-documented in literature and a minor role also in the analyzed model system cannot be excluded.

Oxidation of model Ni-Cr alloys under controlled low  $p_{O_2}$  conditions at a moderate temperature was beneficial to isolate interfacial atomic transport mechanisms during selective oxidation. Several studies of similar model systems in gaseous atmospheres at reduced oxygen partial pressure are also available in the literature for comparison with the observed oxide scales using oxygen isotopic tracers. Especially during confined oxidation along interfaces, the growth of precipitates can severely alter the oxidation response during exposure to reduced oxygen availability<sup>44,52</sup>. A well-established explanation suggests the reduction of GB diffusivity by dissolved C as the main reason for the improved resistance against IG corrosion<sup>53–55</sup>. The alloys used in the present study did not form unwanted precipitates such as carbides. The slightly increased N content in Ni-5Cr (Fig. 6) can be mostly retracted to minor accumulation within the oxide. Nevertheless, the TEM diffraction indicates the expected lattice parameters of Cr<sub>2</sub>O<sub>3</sub>. It can be assumed that the N impurities do not significantly alter the oxidation mechanism. To differentiate internal and external oxidation, Rhines packs were generally adapted in the literature<sup>9,11,50</sup>. The oxide networks along GBs were furthermore reported to be mostly continuous. This aligns well with our results after exposure at significantly lower temperatures (600 °C).

Additionally, the investigation of model compositions with 20 at.% Cr increases the comparability of the results with commercial alloy systems (e.g., Alloy 600). The exact mechanisms of IG attack in Alloy 600 samples during moderate temperature exposure in hydrogenated water or steam are still under debate<sup>21,44,49</sup>. This is unsatisfying since oxidation is considered a precursor event to component failures via more deleterious effects, including stress corrosion cracking<sup>21,45</sup>. A consensus developed that transport fluxes of O and Cr decide if a fast penetrating Cr<sub>2</sub>O<sub>3</sub> network develops along GBs or if the regions remain protected by a protective cap on the surface<sup>44</sup>. The present study proves the immense value that is reached by the combination of APT with oxygen tracer exchange studies. The reduction of complexity comes with the reward of direct access to transport mechanisms on the near-atomic scale. The demonstrated results indicate the potential to address research questions that could not be solved over decades. Admittedly, the insight into oxygen transport of this well-defined model scenario provided a number of additional tasks that can be elegantly addressed with the developed research strategy. For example, its elucidation of the correlation between individual grain boundary characters on the susceptibility to IG attack is of high relevance. For modeling, access to individual diffusivities of GBs is valuable. This is also supported by the recent study in which Poplawsky et al. concluded that O diffusion along alloy GBs must be considered to foresee oxidation resistance during the development of high-temperature alloys<sup>14</sup>.



## METHODS

### High-purity alloys

High-purity Ni-Cr binary alloys were fabricated by SAES Smart Materials. Both elements, Ni and Cr were high-purity precursors leading to an as-cast purity of 0.99x%. The nominal alloy compositions were measured by ICP-MS and APT, and supplemented by glow discharge mass spectroscopy (GDMS) for the low level of impurities (320 appm Fe and 13 appm S being the most significant). Small coupons ( $\approx 8 \times 8 \times 2$  mm) were prepared for oxidation experiments. The faces of the coupons were ground with SiC paper and polished to a mirror-finish with colloidal silica.

### Exposure to environments below Ni/NiO equilibrium

Oxidation exposures at controlled  $p_{O_2}$  were carried out in a vertical furnace equipped with a turbomolecular pump for efficient change of atmosphere. A mixture of CO/CO<sub>2</sub> with a ratio 1:10 leads to an oxygen partial pressure below the dissociation pressure of NiO at 600 °C. The flow rates were controlled by mass flow controllers at high accuracy. At the target temperature, the total pressure in the system remained constant at 800 mbar. Heating and cooling rates were 10 K/min. Baseline exposure to document the expected IG attack had a duration of 1 h. Oxygen isotopic exchange experiments followed a classical two-stage approach. In the first step, the model alloy samples were exposed for 40 min to a mixture of CO/CO<sub>2</sub> mixture with natural isotopic abundances. Subsequently, the atmosphere was changed to a mixture of CO and C<sup>18</sup>O<sub>2</sub> ( $c(^{18}O) = 97\%$ ) with the same ratio (1:10). The sample was oxidized for an additional 80 min, for a total oxidation time of 2 h.

### Material characterization

Scanning electron microscopy (SEM) and site-specific preparation of specimens for transmission electron microscopy (TEM) and APT were accomplished using two dual beam SEM/focused ion-beam (FIB) systems: an FEI Quanta 3D and FEI Helios 3D. SEM imaging was performed at 5 kV in both secondary electron (SE) and backscattered electron (BSE) imaging modes. For sample preparation, oxidized GBs were first protected by a Pt cap deposited by the FIB's gas injection system. FIB lift-outs were then prepared for TEM and APT using well-established protocols<sup>56</sup>. During preparation, the specimens were shaped and/or thinned using a 30 kV Ga<sup>+</sup> ion-beam, followed by a 2 kV Ga<sup>+</sup> ion cleaning procedure to minimize ion-beam damage. For APT samples, the clean-up step lasted until the region of interest (metal/oxide interface) appeared within 100 nm below the specimen apex.

Scanning transmission electron microscopy (STEM) was performed using an aberration (CS) corrected, JEOL ARM200CF operated at 200 keV equipped with a JEOL Centurio energy dispersive spectrometer (EDS) with a 0.9 sR collection angle. Annular dark-field (ADF) data were collected with a convergence angle of 20 mrad and a collection angle ranging from 79–294 mrad. Digital imaging data collection was performed using Gatan Microscopy Suite (GMS) version 3.

Time-of-flight secondary ion mass spectrometry (ToF-SIMS) measurement was performed at Environmental Molecular Sciences Laboratory (EMSL), which is located at Pacific Northwest National Laboratory. A TOF.SIMS5 instrument (IONTOF GmbH, Münster, Germany) was used. Dual-beam interlaced mode depth profiling was used. A 1.0 keV Cs<sup>+</sup> beam was used as the sputtering beam and a 50 keV Bi<sub>3</sub><sup>++</sup> beam was used as the analysis beam for signal collection. The Cs<sup>+</sup> sputtering beam ( $\approx 77$  nA) was scanned over a 300\*300  $\mu\text{m}^2$  area. The Bi<sub>3</sub><sup>++</sup> beam was focused to be about 5  $\mu\text{m}$  diameter with a beam current was about 0.10 pA with a 10 kHz frequency. The Bi<sub>3</sub><sup>++</sup> beam was scanned over an area of 100\*100  $\mu\text{m}^2$  at the Cs<sup>+</sup> sputter crater center.

The APT analysis of oxidized Ni-Cr alloys was limited to sample volumes that included significant oxide below the original sample

surface. Material transport along oxide/metal interfaces was suspected to contribute extensively to the overall oxidation mechanism and was the primary target for APT analyses. APT measurements used a LEAP 4000X HR in laser pulsing mode ( $\lambda = 355$  nm, pulsing frequency 125–250 Hz). The pulse energies were adjusted to 80 pJ to maintain a Cr<sup>++</sup>/Cr<sup>+</sup> ratio of  $\approx 2$ . 3D reconstructions of APT data were performed with the commercial Integrated Visualization and Analysis Software (IVAS) package from Cameca, v 3.8.12. Further analysis and visualization of the reconstructed data were conducted with the open-source software GNU Octave. A custom dedicated toolbox, adapting many routines initially developed by Peter Felfer in MatLab.

### APT data handling

The analysis of APT datasets was conducted in multiple steps. 3D reconstruction of ion positions was performed with the commercial Integrated Visualization and Analysis Software (IVAS) package from Cameca. The visualization of data and all additional analysis were conducted with the open-source software GNU Octave. A dedicated toolbox adapting the general routines suggested by Peter Felfer was implemented for the advanced handling of isotopes within the analyzed data.

### DATA AVAILABILITY

All data that support the results of the present study are available from the corresponding author upon reasonable request.

Received: 12 March 2023; Accepted: 7 July 2023;

Published online: 22 August 2023

### REFERENCES

- Airey, G. P. Microstructural aspects of the thermal treatment of inconel alloy 600. *Metallography* **13**, 21–41 (1980).
- Andresen, P. L. Effects of temperature on crack growth rate in sensitized type 304 stainless steel and alloy 600. *Corrosion* **49**, 714–725 (1993).
- Bruemmer, S. M. & Was, G. S. Microstructural and microchemical mechanisms controlling intergranular stress corrosion cracking in light-water-reactor systems. *J. Nucl. Mater.* **216**, 348–363 (1994).
- Evans, H. E., Donaldson, A. T. & Gilmour, T. C. Mechanisms of breakaway oxidation and application to a chromia-forming steel. *Oxid. Met.* **52**, 379–402 (1999).
- Halvarsson, M., Tang, J. E., Asteman, H., Svensson, J. E. & Johansson, L. G. Microstructural investigation of the breakdown of the protective oxide scale on a 304 steel in the presence of oxygen and water vapour at 600 °C. *Corros. Sci.* **48**, 2014–2035 (2006).
- Wagner, C. Reaktionstypen bei der oxydation von Legierungen. *Z. Elektrochemie* **63**, 772–782 (1959).
- Wagner, C. Theoretical analysis of the diffusion processes determining the oxidation rate of alloys. *J. Electrochem. Soc.* **99**, 369–380 (1952).
- Rhines, F. A metallographic study of internal oxidation in the alpha solid solutions of copper. *Trans. Met. Soc. AIME* **137**, 246–290 (1940).
- Stott, F. H. et al. The transport of oxygen to the advancing internal oxide front during internal oxidation of nickel-base alloys at high temperature. *Solid State Ionics* **12**, 365–374 (1984).
- Martinez-Villafaña, A., Stott, F. H., Chacon-Nava, J. G. & Wood, G. C. Enhanced oxygen diffusion along internal oxide-metal matrix interfaces in ni-al alloys during internal oxidation. *Oxid. Met.* **57**, 267–279 (2002).
- Wood, G. C., Stott, F. H., Whittle, D. P., Shida, Y. & Bastow, B. D. The high-temperature internal oxidation and intergranular oxidation of nickel-chromium alloys. *Corros. Sci.* **23**, 9–25 (1983).
- McIntyre, N. S., Chan, T. C. & Chen, C. Characterization of oxide structures formed on nickel-chromium alloy during low pressure oxidation at 500–600 °C. *Oxid. Met.* **33**, 457–479 (1990).
- Kruska, K., Schreiber, D. K., Olszta, M. J., Riley, B. J. & Bruemmer, S. M. Temperature-dependent selective oxidation processes for Ni-5Cr and Ni-4Al. *Corros. Sci.* **139**, 309–318 (2018).
- Poplawsky, J. D. Measuring oxygen solubility in Ni grains and boundaries after oxidation using atom probe tomography. *Scripta Mater.* **210**, 114411 (2022).

15. Hart, E. On the role of dislocations in bulk diffusion. *Acta Metall. Mater.* **5**, 597 (1957).
16. Frischat, G. H. Mass transport in solids. *Angew. Chem. Int. Edit.* **13**, 384–398 (1974).
17. Basu, S. N. & Halloran, J. W. Tracer isotope distribution in growing oxide scales. *Oxid. Met.* **27**, 143–155 (1987).
18. Harrison, L. G. Influence of dislocations on diffusion kinetics in solids with particular reference to the alkali halides. *Trans. Faraday Soc.* **57**, 1191–1199 (1961).
19. Capell, B. M. & Was, G. S. Selective internal oxidation as a mechanism for intergranular stress corrosion cracking of Ni-Cr-Fe alloys. *Metall. Mater. Trans. A* **38**, 1244–1259 (2007).
20. Persaud, S. Y., Korinek, A., Huang, J., Botton, G. A. & Newman, R. C. Internal oxidation of alloy 600 exposed to hydrogenated steam and the beneficial effects of thermal treatment. *Corros. Sci.* **86**, 108–122 (2014).
21. Volpe, L., Burke, M. G. & Scenini, F. Oxidation behaviour of solution-annealed and thermally-treated Alloy 690 in low pressure H<sub>2</sub>-Steam. *Corros. Sci.* **167**, 108,514 (2020).
22. Pande, C. S., Suenaga, M., Vyas, B., Isaacs, H. S. & Harling, D. F. Direct evidence of chromium depletion near the grain boundaries in sensitized stainless steels. *Scripta Metall. Mater.* **11**, 681–684 (1977).
23. Becker, P., Panasko, M. & Young, D. J. Cyclic oxidation of heat resisting steels. *Oxid. Met.* **64**, 281–301 (2005).
24. Kilner, J. A., Steele, B. C. H. & Ilkov, L. Oxygen self-diffusion studies using negative-ion secondary ion mass spectrometry (SIMS). *Solid State Ionics* **12**, 89–97 (1984).
25. Chater, R. J., Weiser, M. & Virtanen, S. Visualizing ion transport mechanisms through oxide scales grown on mixed nickel- and cobalt-base model alloys at 900 °C using FIB-SIMS techniques. *J. Vac. Sci. Technol.* **36**, 03F116 (2018).
26. Voyshnis, S. et al. Oxide layer growth on nickel-base alloy surfaces in high temperature water and in O<sub>2</sub> studied by ToF-SIMS with isotopic tracers. *Corros. Sci.* **145**, 212–219 (2018).
27. Quadackers, W. J., Elschner, A., Speier, W. & Nickel, H. Composition and growth mechanisms of alumina scales on FeCrAl-based alloys determined by SNMS. *Appl. Surf. Sci.* **52**, 271–287 (1991).
28. Naumenko, D., Gleeson, B., Wessel, E., Singheiser, L. & Quadackers, W. J. Correlation between the microstructure, growth mechanism, and growth kinetics of alumina scales on a FeCrAlY alloy. *Metall. Mater. Trans. A* **38 A**, 2974–2983 (2007).
29. Viskari, L., Hörnqvist, M., Moore, K. L., Cao, Y. & Stiller, K. Intergranular crack tip oxidation in a Ni-basesuper alloy. *Acta Mater.* **61**, 3630–3639 (2013).
30. Rapp, R. The transition from internal to external oxidation and the formation of interruption bands in silver-indium alloys. *Acta Metall. Mater.* **9**, 730–741 (1961).
31. Weiser, M., Schreiber, D. K., Kruska, K., Engelhard, M. H., & Olszta, M. J. Intergranular oxidation and oxygen transport in Ni-20Cr during exposure to model dry and wet oxidation environments. *20th International Conference on Environmental Degradation of Materials in Nuclear Power Systems—Water Reactors, EnvDeg 2021* (Snowmass Village, CO, USA, 2022).
32. Bachhav, M., Danoix, F., Hannyoy, B., Bassat, J. M. & Danoix, R. Investigation of O-18 enriched hematite (*alpha*-Fe<sub>2</sub>O<sub>3</sub>) by laser assisted atom probe tomography. *Int. J. Mass Spectrom.* **335**, 57–60 (2013).
33. Felfel, P., Scherrer, B., Demeulemeester, J., Vandervorst, W. & Cairney, J. Mapping interfacial excess in atom probe data. *Ultramicroscopy* **159**, 438–444 (2015).
34. Felfel, P. & Cairney, J. Advanced concentration analysis of atom probe tomography data: local proximity histograms and pseudo-2D concentration maps. *Ultramicroscopy* **189**, 61–64 (2018).
35. Schreiber, D. K. et al. Examinations of oxidation and sulfidation of grain boundaries in alloy 600 exposed to simulated pressurized water reactor primary water. *Microsc. Microanal.* **19**, 676–687 (2013).
36. Stott, F. H. & Wood, G. C. Internal oxidation. *Mater. Sci. Tech-Lond* **4**, 1072–1078 (1988).
37. Langelier, B., Persaud, S. Y., Newman, R. C. & Botton, G. A. An atom probe tomography study of internal oxidation processes in Alloy 600. *Acta Mater.* **109**, 55–68 (2016).
38. Brueckman, A., Emmerich, R. & Mrowec, S. Investigation of the high-temperature oxidation of Fe-Cr alloys by means of the isotope <sup>18</sup>O. *Oxid. Met.* **5**, 137–147 (1972).
39. Shida, Y., Wood, G. C., Stott, F. H., Whittle, D. P. & Bastow, B. D. Intergranular oxidation and internal void formation in Ni-40% Cr alloys. *Corros. Sci.* **21**, 581–597 (1981).
40. Weiser, M., Chater, R. J., Shollock, B. A. & Virtanen, S. Transport mechanisms during the high-temperature oxidation of ternary Equation 11 Co-base model alloys. *npj Mater. Degrad.* **3**, 33 (2019).
41. Volpe, L., Burke, M. G. & Scenini, F. Understanding the role of diffusion induced grain boundary migration on the preferential intergranular oxidation behaviour of alloy 600 via advanced microstructural characterization. *Acta Mater.* **175**, 238–249 (2019).
42. Balluffi, R. W. & Cahn, J. W. Mechanism for diffusion induced grain boundary migration. *Acta Metall. Mater.* **29**, 493–500 (1981).
43. Shen, Z., Karamched, P., Arioka, K. & Lozano-Perez, S. Observation and quantification of the diffusion-induced grain boundary migration ahead of SCC crack tips. *Corros. Sci.* **147**, 163–168 (2019).
44. Volpe, L., Bertali, G., Scenini, F. & Burke, M. G. Effect of temperature on the preferential intergranular oxidation susceptibility of thermally-treated Alloy 600. *Corros. Sci.* **207**, 110565 (2022).
45. Bruemmer, S. M., Olszta, M. J., Toloczko, M. B. & Schreiber, D. K. Grain boundary selective oxidation and intergranular stress corrosion crack growth of high-purity nickel binary alloys in high-temperature hydrogenated water. *Corros. Sci.* **131**, 310–323 (2018).
46. Langelier, B. et al. Effects of boundary migration and pinning particles on intergranular oxidation revealed by 2D and 3D analytical electron microscopy. *Acta Mater.* **131**, 280–295 (2017).
47. Thomas, L. E. & Bruemmer, S. M. High-resolution characterization of intergranular attack and stress corrosion cracking of alloy 600 in high-temperature primary water. *Corrosion* **56**, 572–587 (2000).
48. Bertali, G., Scenini, F. & Burke, M. G. The intergranular oxidation susceptibility of thermally-treated alloy 600. *Corros. Sci.* **114**, 112–122 (2017).
49. Persaud, S. Y. et al. Characterization of initial intergranular oxidation processes in alloy 600 at a sub-nanometer scale. *Corros. Sci.* **133**, 36–47 (2018).
50. Bradley, L., Wood, G. C. & Stott, F. H. The effects of stress on the internal oxidation of Ni-Cr and Ni-Al alloys. *Mater. Sci. Forum.* **251-254**, 341–348 (1997).
51. Persaud, S. Y., Ramamurthy, S. & Newman, R. C. Internal oxidation of alloy 690 in hydrogenated steam. *Corrosion Science* **90**, 606–613 (2015).
52. Bertali, G., Burke, M. G., Scenini, F. & Huin, N. The effect of temperature on the preferential intergranular oxidation susceptibility of alloy 600. *Metall. Mater. Trans. A* **49**, 1879–1894 (2018).
53. Moulin, P., Huntz, A. M. & Lacombe, P. Influence du carbone sur la diffusion du chrome et du nickel en volume et dans les joints de grains de l'alliage Ni-Cr 80/20. *Acta Metall. Mater.* **27**, 1431–1443 (1979).
54. Hertzberg, J. L. & Was, G. S. The effect of carbon on grain boundary diffusivity in Ni-16Cr-9Fe alloys. *Scripta Metall. Mater.* **33**, 1193–1199 (1995).
55. Giggins, C. S. & Pettit, F. S. Corrosion of metals and alloys in mixed gas environments at elevated temperatures. *Oxid. Met.* **14**, 363–413 (1980).
56. Thompson, K. et al. In situ site-specific specimen preparation for atom probe tomography. *Ultramicroscopy* **107**, 131–139 (2007).

## ACKNOWLEDGEMENTS

This was supported by the U.S. Department of Energy (DOE) Office of Science, Basic Energy Sciences Materials Science and Engineering Division (FWP 56909). MW acknowledges scientific and financial support from the Deutsche Forschungsgemeinschaft (DFG) through a 1-year research fellowship. Additional support was provided by the EAM, an FAU Competence Center, through Starting Grant EAM-SG21-3. A portion of this research was performed on a project award (10.46936/cpcy.proj.2019.51178/60006716) from the Environmental and Molecular Sciences Laboratory, a DOE Office of Science User Facility sponsored by the Biological and Environmental Research program and located at Pacific Northwest National Laboratory (PNNL). PNNL is a multiprogram national laboratory operated by Battelle for the U.S. DOE under Contract DE-AC05-79RL01830.

## AUTHOR CONTRIBUTIONS

M.W. and D.K.S. designed the experiments. M.W. and M.H.E. conducted the two-stage exposures. M.J.O. elucidate the oxidized cross-sections with TEM. M.W. and D.K.S. conducted sample preparation and APT. The initial outline of the manuscript was done by M.W. and D.K.S. All authors discussed and contributed to the writing of the paper.

## FUNDING

Open Access funding enabled and organized by Projekt DEAL.

## COMPETING INTERESTS

The authors declare no competing interests.

## ADDITIONAL INFORMATION

**Supplementary information** The online version contains supplementary material available at <https://doi.org/10.1038/s41529-023-00387-w>.

**Correspondence** and requests for materials should be addressed to Martin Weiser.

**Reprints and permission information** is available at <http://www.nature.com/reprints>

**Publisher's note** Springer Nature remains neutral with regard to jurisdictional claims in published maps and institutional affiliations.



**Open Access** This article is licensed under a Creative Commons Attribution 4.0 International License, which permits use, sharing, adaptation, distribution and reproduction in any medium or format, as long as you give appropriate credit to the original author(s) and the source, provide a link to the Creative Commons license, and indicate if changes were made. The images or other third party material in this article are included in the article's Creative Commons license, unless indicated otherwise in a credit line to the material. If material is not included in the article's Creative Commons license and your intended use is not permitted by statutory regulation or exceeds the permitted use, you will need to obtain permission directly from the copyright holder. To view a copy of this license, visit <http://creativecommons.org/licenses/by/4.0/>.

© The Author(s) 2023